FINAL REPORT

High Fidelity Antenna Model Development (HFAM) for Creation of CAT-I Siting Criteria

Daniel N. Aloi, Ph.D.
Principal Investigator

July 2007

Electrical and Computer Engineering Department
School of Engineering and Computer Science
Oakland University
Rochester, Michigan

Prepared under:
Federal Aviation Administration Research Grant 2003-G-001
Federal Aviation Administration Cooperative Agreement 02-P0073

TABLE OF CONTENTS

LIST OF FIGURES

LIST OF TABLES

1. Introduction

The Local Area Augmentation System's (LAAS) Ground Facility (LGF) requires the use of an integrated multipath limiting antenna (IMLA). In support of the LAAS, several projects were performed under Federal Aviation Administration Cooperative Agreement 2003-G-001. These projects can be developed into three research tasks:

1. High Fidelity Antenna Model Development (HFAM)
2. Reference Receiver Site Data Collections with Dual-Frequency IMLA
3. Anti-Jam Approaches for Multipath Limiting Antenna.

Each of these research tasks is summarized below. Detailed descriptions are provided in Chapters 2 through 4.

High Fidelity Antenna Model Development (HFAM)
The integrated multipath limiting antenna (IMLA) is a proposed antenna in Local Area Augmentation System (LAAS) Ground Facilities (LGF). Non-Zero Mean (NZM) biases in the corrections formed at each reference receiver site (RRS) ground installation present an integrity risk to LAAS. The IMLA induced NZM biases were quantified via simulation through the development of a HFAM. The HFAM was validated against antenna range measurements and GPS field data collections. The validated HFAM was then used to assess the IMLA's NZM contribution to the overall integrity risk of LAAS for Cat I installations.

An additional HFAM of the dual-frequency IMLA was also to be developed but has been put on hold due to the status of the LAAS program. The following publications resulted in this area of the project [1, 2, 3].

Reference Receiver Site Data Collections with Dual-Frequency IMLA
A RRS was installed at Pontiac International Airport in Waterford, Michigan to collect continuous GPS data from a dual-frequency IMLA connected to a dual-frequency GPS receiver. The data was processed to quantify the mean and standard deviation of the code-minus-carrier (CMC) data as a function of elevation and azimuth angle. A dual-frequency antenna enables the removal of the effects of the ionosphere from the code phase and accumulated carrier phase measurements produced by a GPS receiver. These results are important for Cat II/III installations because LAAS will be used internationally. WAAS has been a proposed solution to eliminate the need for dual-frequency antennas. This solution is not possible for countries that are located outside of the WAAS coverage area. In addition, this data was intended to be used to validate the HFAM of the dual-frequency IMLA.

Anti-Jam Approaches for Multipath Limiting Antenna (MLA)
Intentional and unintentional interference are concerns that impact integrity, continuity of service and availability at LAAS installations for Cat II/III service. Two beam\null-steering algorithms for the MLA were investigated to assess the improvement in availability under interference conditions. The following publications resulted from this effort [4,5 , 6, 7, 8, 9].

2. High Fidelity Antenna Model Development

The High Fidelity Antenna Model (HFAM) is an electromagnetics model of the integrated multipath limiting antenna (IMLA) produced by dBSystems, Inc. Section 2.1 describes the physical design for the IMLA. While Section 2.2 describes the HFAM of the IMLA and Section 2.4 and Section 2.5 shows the validation results for the MLA and HZA portions of the HFAM of the IMLA, respectively.

2.1 IMLA Physical Architecture

The IMLA consists of a multipath limiting antenna (MLA) that provides coverage in elevation from 0° - 35° and a high zenith antenna (HZA) that provides coverage in elevation from 35° to 90°. Both the MLA and the HZA provide omni-directional coverage in the azimuth directions. A description of the MLA and the HZA are provided in Section 2.1.1 and Section 2.1.2, respectively.

2.1.1 Multipath Limiting Antenna (MLA)

The MLA was designed to mitigate ground multipath ranging error, and accomplishes this by utilizing an array of stacked vertically polarized radiating elements. The amplitudes and phases of the excitation signals for each of the radiating elements are chosen to shape the aggregate radiation pattern in a manner that focuses energy above the antenna horizon while minimizing it below the antenna horizon. Error in GPS measurement due to ground multipath is thereby mitigated, as the magnitude of the ground reflected signal arriving at an antenna is reduced with respect to that that of the direct signal - the ratio of the amplitudes of the two signals strongly dictates the magnitude of the multipath error. To date, two models of the MLA have been developed for GPS signal reception at the LGF: a 14-element array, and a 16-element array. This section describes the modeling and validation of the 14-element version.

The fundamental radiating element of the MLA is a dipole cup, the length of which is a quarter of a GPS L1 wavelength. The usage of the dipole cup, rather than a wire element contributes to the wide bandwidth of the antenna. A photograph of the dipole cup array and its feed distribution circuit is illustrated in Figure 1.

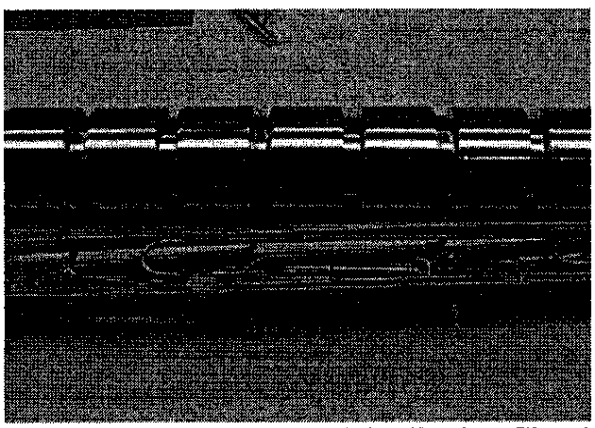

Figure 1. Radiating structure and Feed Distribution Circuit of the MLA.

A feed distribution circuit is contained at the base of the antenna to control the signal amplitude and phase that is fed to each radiating element. The feed distribution circuit is comprised of Wilkinson Power Splitters and RF cable sections. The amplitude is controlled mainly by the Wilkinson Power Splitters while the phase is controlled by the RF cable length that commences at the feed distribution circuit and terminates at a dipole cup to controls the phase of signal. The feed cable ultimately excites a dipole cup at four points spaced equally around its circumference. This is accomplished as follows: power is first split within the support tube structure; the two outputs of the RF splitter are fed to two points that are 180 degrees apart from each other on the support structure within the dipole cup; each of these two signals are further split two-ways, and the four resulting RF outputs are attached to four points on the dipole cup, spaced 90 degrees with respect to each other along the circumference. The dipole cups are also uniformly spaced in the vertical direction. Ideally, all four points should sense the same amplitude and phase feed for a given dipole. The signal specifications for each dipole cup are determined by the antenna manufacturer and are proprietary. The support structure, radiating dipole cups, feed distribution circuit, and RF cables are then enclosed within a cylindrical radome for environmental protection.

2.1.2 High Zenith Antenna (HZA)

The HZA, shown in Figure 2 and Figure 3, utilizes several antenna technologies in order to meet the gain D/U requirements. The key technologies incorporated are listed below:

a. The radiating element consists of two orthogonal cross-v dipoles that operate at a center frequency of 1575.42 MHz, with a quarter-wavelength balun connected to the dipole feeds for impedance matching. A 90-degree power combiner is connected at the antenna feeds in order to combine the signals in an RHCP sense. The cross-v dipole is electrically symmetric and has a large bandwidth, thereby exhibiting a fixed phase center and minimal group delay.
b. A flat conductive, reflecting counterpoise oriented orthogonal to the vertical axes of the antenna and electrically connected to the cross-v dipoles.
c. A shaped concave reflector electrically connected to the counterpoise. The shaped reflector is used to minimize the antenna gain at lower elevation angles and maximize it at higher elevation angles.
d. A beam forming piece of RF absorbing material that provides controlled positive angle radiation through the use of it's shaped inside and outside contours that control the broadside and negative angle portions of the radiation pattern. The RF absorbing material possesses homogeneous dielectric properties.
e. A vertically oriented, quarter wave, RF-choke which aids in the suppression of surface waves that exists on the microwave absorbing material.

A low noise amplifier (LNA) is connected at the output of the antenna to amplify weak GPS signals, followed by an isolator to absorb any reflection due to mismatch between the RF cable and the GPS receiver. The antenna, LNA, and isolator are mounted on an aluminum plate and enclosed in a fiber-glass radome for environmental protection.

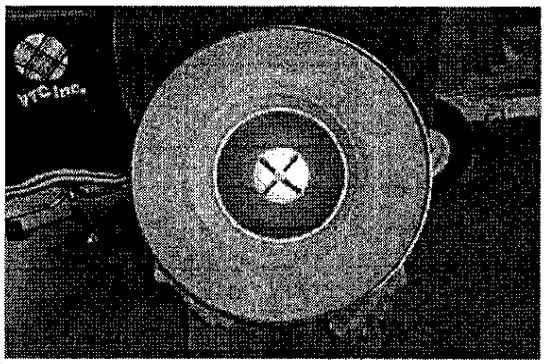

Figure 2. Top-View of an HZA Illustrating the Cross-V Dipole Radiating Mechanism.

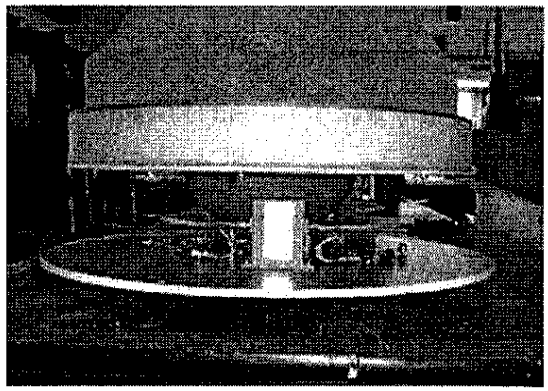

Figure 3. Side-View of an HZA Showing the Bowl-Shaped Reflector, Flat Counterpoise, RF Absorbing Material, and RF Choke.

2.2 HFAM Description

It was determined that a two-stage approach would be needed to model the MLA. The first stage models the feed network of the MLA using a high frequency circuit simulator, SPICE, for each of the 14 RF paths to the corresponding radiating dipole cups. Each RF path in the SPICE model was terminated with the equivalent impedance of a dipole cup. The complex excitation voltages for each dipole cup at the output of the SPICE model were then used as excitations to the model of the radiating structure using FEKO. Finally, the resulting far-field electric fields from the FEKO model are input to the Post-Processing Module to compute the desired-to-undesired gain ratio, phase center variation, and group delay as a function of frequency, elevation, or azimuth. The HZA does not have an extensive feed network and its model was done exclusively within FEKO. Figure 4 illustrates the final FEKO model of the IMLA. Due to the large size of this structure, its validation for the MLA and HZA portions of the IMLA were conducted independently.

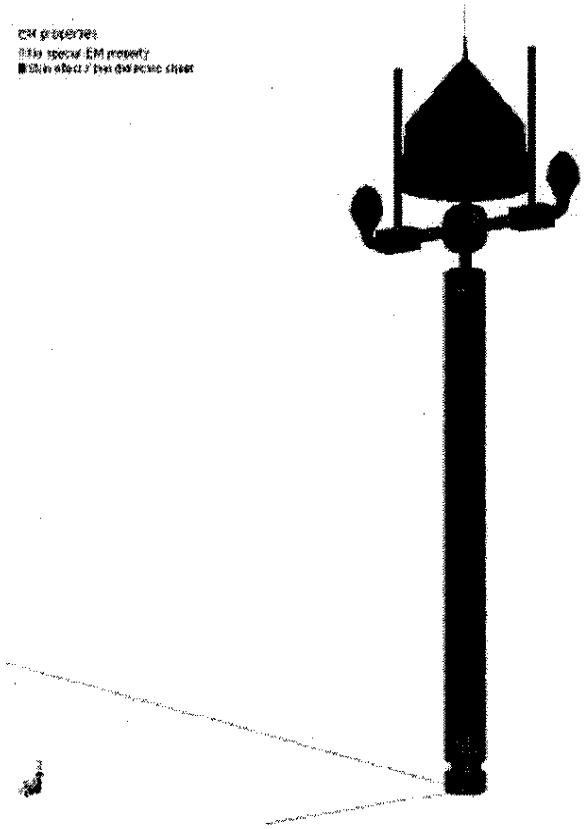

Figure 4: A Three Dimensional Full Wave Field Solver (FEKO) Based on the Method of Moments was Utilized to Construct the IMLA and Solve for its Corresponding Complex Radiation Pattern.

2.2.1 MLA Portion

The feed distribution circuit consists of copper coaxial cables with a Teflon dielectric material ($\varepsilon r = 1.93$) and Wilkinson transformers with brass conductive cables. Such transformers are formed by using air filled coaxial cables with delta connected termination resistors at the output of each. Figure 5 shows a transmission line model. The distributed model can be characterized by and RLGC combination, each represented as a function of length.

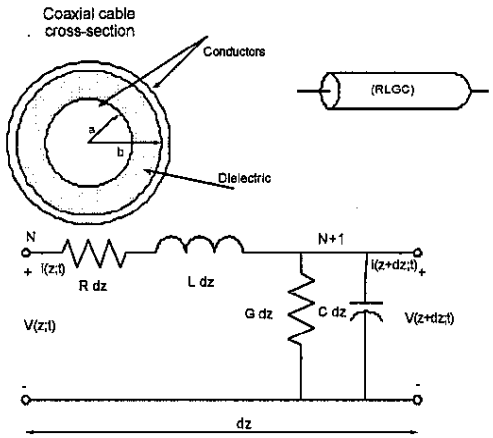

Figure 5: Coaxial Line Model Used in this Research.

Figure 6 shows a single path from the RF input of the MLA to the input of the fork power splitter, represented by RL.

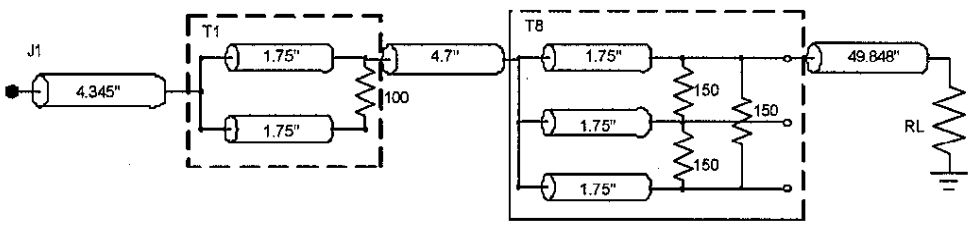

Figure 6: MLA Feed Network from RF Input to Dipole 6.

The transformers combine signals from various paths with certain ratios and phases to yield the desired pattern. To yield the desired gain pattern for the MLA along with the minimum PCV and GD, such a network has to be modeled and designed carefully. Modeling of the coaxial transmission lines and Wilkinson transformers were based on calculating the RLGC values for each section as a function of length using the relationships in Equation 1 thru Equation 4.

$$R = \frac{R_s}{2\pi}\left(\frac{1}{a}+\frac{1}{b}\right) \ \Omega/m, \text{ where } R_s = \sqrt{\pi f \mu_c / \sigma_c} \tag{1}$$

$$L = \frac{\mu_c}{2\pi}\ln\left(\frac{b}{a}\right) \quad H/m \tag{2}$$

$$G = \frac{2\pi\sigma_d}{\ln\left(\frac{b}{a}\right)} \quad S/m \tag{3}$$

$$C = \frac{2\pi\varepsilon_c}{\ln\left(\frac{b}{a}\right)} \qquad F/m \tag{4}$$

where, a and b are the diameters of the inner and outer conductors, respectively, f is the frequency of operation, μ is the permeability, σ is the conductivity and ε_r is the relative permittivity of the material. The subscripts c and d denote conductor and dielectric, respectively.

The complex propagation constant of a transmission line is given by Equation 5.

$$\gamma = \alpha + j\beta \tag{5}$$

where,

$$\alpha = \mathrm{Re}\{\gamma\} = \mathrm{Re}\left\{\sqrt{(R + j\omega L)(G + j\omega C)}\right\} \tag{6}$$

$$\beta = \mathrm{Im}\{\gamma\} = \mathrm{Im}\left\{\sqrt{(R + j\omega L)(G + j\omega C)}\right\} \tag{7}$$

The characteristic impedance of the transmission line can be found using.

$$Z_0 = \sqrt{\frac{(R + j\omega L)}{(G + j\omega C)}} \tag{8}$$

The feed network circuit was modeled using PSPICE to reflect the nominal physical design by dBSystems, Inc. The excitation source was a sinusoidal waveform applied to the MLA RF feed point. The 14 outputs of the feed network circuit were terminated at the input to the 14 power splitters that reside within the support tube structure. The outputs of the feed network are stored in complex format Vn (amplitude and phase) for each of the 14 ports, and recorded at f0 = 1575.42 MHz, f1 = 1574.42 MHz and f2 = 1576.42 MHz. These complex excitations are then passed to a FEKO model of the radiating structure of the MLA that computes the complex electric far-field values as a function of frequency and spherical coordinates.

The output of the network was tuned to match the actual complex feed levels that were provided by the manufacturer at f0. Tuning reflects the necessary adjustments in the nominal design of the feed distribution circuit in order to ensure the relative amplitude and phase of the complex excitation voltages match the theoretical values. The phase is initially adjusted on the final section of the coaxial cables to match the phases and then the Wilkinson Transformer tube diameters are adjusted in order to arrive at the correct relative amplitudes. This same process is performed during manufacturing and generally results in a final design that does not exactly match the nominal design. Once the PSPICE model of the feed distribution circuit is calibrated at L1, then the PSPICE model is excited at two additional frequencies L1 +/ 1 MHz. The feed network parameters (the frequency dependent ones) were altered for these two frequencies to

reflect the effect of frequency change. The change of the complex excitations affects the MLA parameters: desired-to-undesired gain ratio, phase center variation and group delay.

Table 1: Illustrates the Values of the Parameters used in the Model.

parameter	value
ϵ_r (Teflon)	1.93
σ_c (copper)	5.8×10^7 S/m
σ_c (brass)	1.7×10^7 S/m
σ_d	7.8×10^{-4} S/m
μ_c	1

Table 2: Tuning Process Results as a Percentage of Error Relative to Theoretical Values.

output	amplitude (%)	phase (%)
D1	0	0.187
D2	0.218	-0.013
D3	-0.27	-0.113
D4	-1.299	0.159
D5	-1.314	0.0199
D6	0.501	0.069
D7	-0.344	0
D8	0	0
D9	0.34	0.0139
D10	0.379	0.066
D11	1.227	0.17
D12	0.305	-0.14
D13	1.453	0.108
D14	0	0.054

The MLA was modeled to operate in a frequency band of 1575.42 ± 1 MHz. The entire physical structure of the MLA was modeled using triangular basis functions of edge lengths $\lambda/12$. In addition, the four feed points on each of the 14 dipole cups were modeled as a single wire segment of length $\lambda/20$. These selections resulted in 64 metallic wire segments and 32,352 triangles. A dual-processor Pentium 4 CPU (2.8 GHz) with 4 GB of RAM was used in the modeling of the 14-element single-wall radome version, resulting in a total runtime for a single frequency of 2.43 hours.

The backbone of the MLA is a cylindrical support tube structure, which is utilized to hold the quarter-wave radiating dipole cups in place. The hollow center contains the feed wires that begin from the amplitude and phase feed structure and terminate at each radiating dipole cup pair. The support tube is modeled with conductive dielectric patches of triangle edge length $\lambda/12$.

The 14-element MLA, of course contains fourteen radiating quarter-wave dipole cup pairs. The exact physical dimensions of these dipole cup pairs were obtained from the antenna manufacturer, and were modeled using conductive triangles with edge lengths of $\lambda/12$.

Furthermore, the space between the two cups that comprise each dipole pair was faithfully reproduced, along with the inter-element spacing between each dipole cup pair. As discussed earlier, each radiating dipole element is fed at four distinct points spaced 90-degrees apart along the circumference of the top dipole cup. The specific amplitude and phase parameters for each of the fourteen elements are attained using a combination of cabling and a feed distribution circuit that is located at the base of the antenna (Figure 7).

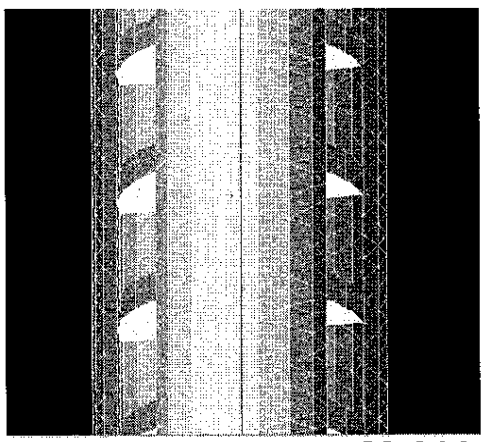

Figure 7: Illustration of a Meshed MoM Antenna Model for the 14-element MLA.

Lastly, the radome is a dielectric material possessing fixed thickness. One method to model the radome is using a volume of dielectric cuboids, but this approach leads to the difficulty of attaching volume basis functions to surface basis functions. Another option is to model the boundary surfaces of the radome with dielectric triangular basis functions and define the contained volume as a dielectric medium, following which the appropriate electrical and magnetic properties of the dielectric surface triangles and the dielectric medium can be assigned. This approach was not taken because of computer memory concerns (19,010 triangles). The approach adopted instead was the utilization of the skin affect approximation in which the physical dimensions of the radome were modeled using surface triangles. The electrical properties for the triangles were then chosen along with a finite thickness. This approach saved memory (9,505 triangles) without sacrificing accuracy.

2.2.2 HZA Portion

In the case of the HZA, the MoM approach alone was used by FEKO to model the entire antenna, following which the RHCP and left-hand circular polarization (LHCP) gains from the electric field components were computed. The HZA was modeled to operate in the frequency range 1575.42 ± 1 MHz. The wire segment and triangle edge lengths were chosen to be $\lambda/15$ and $\lambda/10$, respectively. These selections resulted in 72 metallic wire segments and 8587 triangles (6461 metallic and 2116 dielectric). A Pentium 4 CPU (2.66 GHz) with 1 GB of RAM was used in the HZA modeling effort. The physical and electrical specifications incorporated into the HZA model are described in the remainder of this section.

The cross-v dipoles were modeled as solid metallic wires, although they are in reality hollow cylinders. The wire segment lengths were chosen to be $\lambda/15$. The concave shaped reflector is modeled as a spherical section. This deviates slightly from the actual physical design but was as

close as could be attained using the FEKO geometry meshing tool. The concave shaped reflector was modeled as a conductive surface comprised of triangles with edge lengths of $\lambda/10$.

The flat counterpoise is a circular disc that mates with the top edge of the concave shaped reflector. This section was also modeled as a conductive surface comprised of triangles possessing an edge length of $\lambda/10$. The RF absorbing section that is used to shape the radiation pattern is physically a homogeneous dielectric volume. It is imperative when working with MoM to maintain a solid connection point between all adjacent basis functions (wire segments, surface triangles, and volume cuboids) failing which the solver assumes the existence of discontinuity. The RF absorbing section was initially modeled as a volume comprised of cuboids, with the dielectric constant and loss tangent for each of the cuboids comprising the volume set to a specified value. The problem with this approach was that the cuboids on the bottom of the RF absorbing material could not be electrically attached to the surface triangles of the flat counterpoise.

An alternate approach was adopted in which the outside surface of the RF absorbing material was modeled with surface triangles. The surface triangles and the volume underneath the surface of the RF absorbing material were then modeled as dielectrics with appropriate values for relative dielectric constant and loss tangent. The surface triangles had edge lengths of $\lambda/10$. The relative dielectric constant and loss tangent values of the RF absorbing material are proprietary and are therefore not listed in this paper.

The RF choke is a circular channel that connects to the exterior of the RF absorbing material section. It is made of fiberglass but possesses a conductive layer of coating. The purpose of the RF choke is to reduce the impact of stray surface currents that reside along the surface of the RF absorbing material by presenting high impedance on contact with the RF choke. As the version of FEKO used for the modeling effort is unable to model coated conductors, the RF choke was modeled as three separate conductive surfaces.

Lastly, the radome is a dielectric material possessing fixed thickness. This was modeled using the skin affect approximation in which the physical dimensions of the radome were modeled using surface triangles. The electrical properties for the triangles were assigned along with a finite thickness for the material. These parameters are again proprietary, and are therefore not listed in this paper.

The bottom plate was modeled as a conductive surface with triangle edge lengths of $\lambda/10$. The effect of active elements that follow the antenna, which include an LNA, a 90-degree power hybrid combiner, an isolator, and an L1-band pass filter were not included in the model.

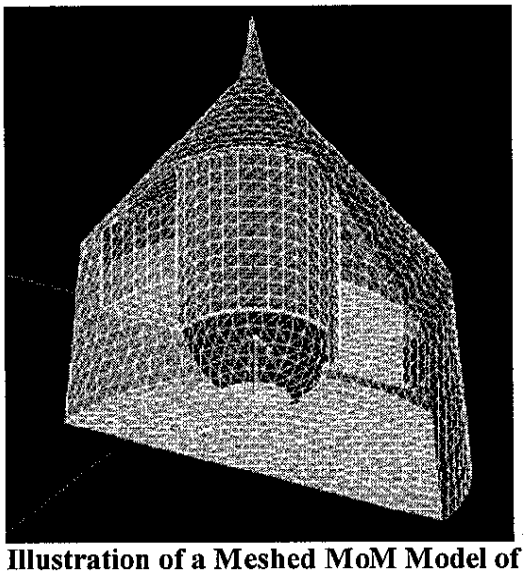

Figure 8: Illustration of a Meshed MoM Model of the HZA.

2.3 Post-Processing Module (MATLAB)

A MATLAB script was written to calculate the desired-to-undesired gain ratio, phase center variation, and group delay from the complex electric far-field data produced at the output of the FEKO models of the MLA and the HZA. The complex electric far-field vector is comprised of a VLP electric field and a horizontal linear polarization (HLP) electric field as defined in Equation 9.

$$\vec{E}_{TOTAL}(\theta_{EL},\theta_{AZ}) = \vec{E}_{VLP}(\theta_{EL},\theta_{AZ}) + \vec{E}_{HLP}(\theta_{EL},\theta_{AZ}) \tag{9}$$

where θ_{EL} is the SV elevation angle with respect to the local horizon; θ_{AZ} the SV azimuth angle with respect to local north; the $\vec{E}_{TOTAL}(\theta_{EL},\theta_{AZ})$ total electric field vector as a function of θ_{EL} and θ_{AZ}; $\vec{E}_{VLP}(\theta_{EL},\theta_{AZ})$ the VLP component of the complex electric field as a function of θ_{EL} and θ_{AZ}; and $\vec{E}_{HLP}(\theta_{EL},\theta_{AZ})$ the HLP component of the complex electric field as a function of θ_{EL} and θ_{AZ}.

From the fundamental electric field components defined in Equation 9, the electric field components corresponding to RHCP and LHCP can be defined as

$$\vec{E}_{RHCP}(\theta_{EL},\theta_{AZ}) = \vec{E}_{VLP}(\theta_{EL},\theta_{AZ}) + j\vec{E}_{HLP}(\theta_{EL},\theta_{AZ}) \tag{10}$$

$$\vec{E}_{LHCP}(\theta_{EL},\theta_{AZ}) = \vec{E}_{VLP}(\theta_{EL},\theta_{AZ}) - j\vec{E}_{HLP}(\theta_{EL},\theta_{AZ}) \tag{11}$$

where, $\vec{E}_{RHCP}(\theta_{EL},\theta_{AZ})$ is the RHCP component of the electric field vector as a function of θ_{EL} and θ_{AZ}; and $\vec{E}_{LHCP}(\theta_{EL},\theta_{AZ})$ is the LHCP component of the electric field vector as a function of θ_{EL} and θ_{AZ}.

Furthermore, the electric field vectors described in Equation 9, Equation 10, and Equation 11 for various states of polarization can be partitioned into real and imaginary parts, as follows:

$$\vec{E}(\theta_{EL},\theta_{AZ}) = \left(\vec{E}_{real}(\theta_{EL},\theta_{AZ}) + j\vec{E}_{imaginary}(\theta_{EL},\theta_{AZ})\right) \tag{12}$$

where $\vec{E}(\theta_{EL},\theta_{AZ})$ is the complex electric field vector for an arbitrary state of polarization; $\vec{E}_{real}(\theta_{EL},\theta_{AZ})$ is the real portion of the electric field as a function of θ_{EL} and θ_{AZ}, and $\vec{E}_{imaginary}(\theta_{EL},\theta_{AZ})$ is the imaginary portion of the electric field as a function of θ_{EL} and θ_{AZ}.

The magnitude and phase of the electric field, as described in Equation 12, can be calculated according to Equation (13) and Equation (14), respectively.

$$\left|\vec{E}(\theta_{EL},\theta_{AZ})\right| = \sqrt{\left(\vec{E}_{real}(\theta_{EL},\theta_{AZ})\right)^2 + \left(\vec{E}_{imaginary}(\theta_{EL},\theta_{AZ})\right)^2} \tag{13}$$

and

$$\angle\vec{E}(\theta_{EL},\theta_{AZ}) = \tan^{-1}\left(\frac{\vec{E}_{imaginary}(\theta_{EL},\theta_{AZ})}{\vec{E}_{real}(\theta_{EL},\theta_{AZ})}\right) \tag{14}$$

Using this, the gain and phase function of the MLA radiation pattern are obtained as listed in Equation 15 and Equation 16, respectively.

$$G_{VLP}(\theta_{EL},\theta_{AZ}) = \frac{2\pi\left|\vec{E}_{VLP}(\theta_{EL},\theta_{AZ})\right|^2}{\eta_0} P_{source} \tag{15}$$

$$\angle\vec{E}_{VLP}(\theta_{EL},\theta_{AZ}) = \tan^{-1}\left(\frac{\vec{E}_{VLP,imaginary}(\theta_{EL},\theta_{AZ})}{\vec{E}_{VLP,real}(\theta_{EL},\theta_{AZ})}\right). \tag{16}$$

In the following section, equations pertaining to the carrier and code PCV and antenna gain D/U are listed.

2.3.1 Phase Center Variation (PCV)

It is important to determine the phase center of the MLA since measurements from the antennae have to be translated to a common reference point corresponding to each IMLA site. The MLA is known to exhibit phase center variation as a function of elevation angle, making it necessary to characterize this behavior and correct for it in order to obtain a constant antenna phase center irrespective of the signal angle-of-arrival.

The carrier phase center variation for the MLA model is calculated as described in Equation17.

$$PCV_{VLP}^{MLA}(\theta_{EL},\theta_{AZ}=const) = \left\{ unwrap\left[\angle\vec{E}_{VLP}^{MLA}(0\le\theta_{EL}\le 35,\theta_{AZ}=const)\right] - unwrap\left[\angle\vec{E}_{VLP}^{MLA}(\theta_{EL}=0,\theta_{AZ}=const)\right] \right\}. \tag{17}$$

The intended coverage area for the MLA in the LAAS architecture is between 0 and 35 degrees in elevation with respect to the local horizon, and omni-directional in azimuth.

2.3.2 Group Delay (GD)

Group delay is a measure of the delay experienced by a narrow-band signal traveling through the medium. Group delay is experienced only if the antenna's phase response is a function of frequency, and its estimation necessitates phase function at two different frequencies about the L1 center frequency. Group delay for the modeled antennae can be calculated corresponding to any elevation and azimuth as

$$GD(\theta_{EL},\theta_{AZ})=\frac{d\phi}{d\omega}= \\ 100\bullet c\bullet\frac{\left[\phi_{(L1+\Delta)}(\theta_{EL},\theta_{AZ})-\phi_{(L1)}(\theta_{EL},\theta_{AZ})\right]}{\left[\omega_{(L1+\Delta)}-\omega_{(L1)}\right]}\ [\text{cm}] \tag{18}$$

2.3.3 Desired-to-Undesired Gain Ratio (D/U)

Gain D/U is a quantity that characterizes an antenna's ability to impact multipath error that may surface due to reflections from the earth. The Gain D/U expression is formed by subtracting the gain in the direction of the multipath signal from that in the direction of the direct signal. This difference represents the relative amplitude of the multipath signal with respect to that of the direct signal, due solely to the antenna gain pattern. This, in conjunction with the GPS receiver tracking loop architecture, is used to limit peak multipath error.

$$D\backslash U(\theta_{EL},\theta_{AZ})= \\ G_{DIRECT}(\theta_{EL},\theta_{AZ})[\text{dB}]-G_{MP}(\theta_{EL},\theta_{AZ})[\text{dB}] \tag{19}$$

2.4 MLA HFAM Validation Results

Reference data for the validation of the models described in this paper was obtained from antenna range measurements performed at dB Systems Inc., Utah, where exists a free space antenna range facility that can adjust the elevation and azimuth angles of the antenna under test with respect to a linearly polarized transmitting source. A network analyzer was utilized to record amplitude and phase measurements at a particular frequency and spatial orientation of each antenna under test.

The fidelity of the electromagnetic model of the MLA was first assessed in terms of the vertical gain pattern (between -40.0 and +40.0 degrees) and gain D/U (correspondingly 0.0 to 40.0 degrees) obtained. Since the back lobes of the MLA are highly sensitive to small adjustments in the amplitude and phase parameters of the 14 radiating elements, gain patterns for 20 different MLAs were measured in order to serve as a reference. The measured gain patterns of these 20 different units are shown in Figure 9.

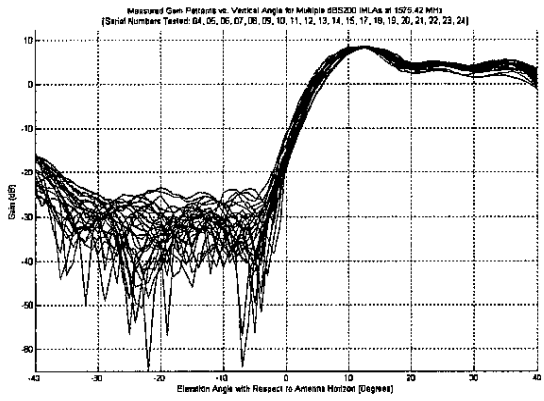

Figure 9. Ensemble gain plots as a funtion of elevation angle for 20 different 14-element MLAs.

The mean and standard deviation of the 20 data samples at each elevation angle between -40 and +40 degrees were calculated from the measured data, and the mean and +/- two-sigma of the measurements are plotted in Figure 10, along with the gain pattern of the FEKO modeled 14-element MLA.

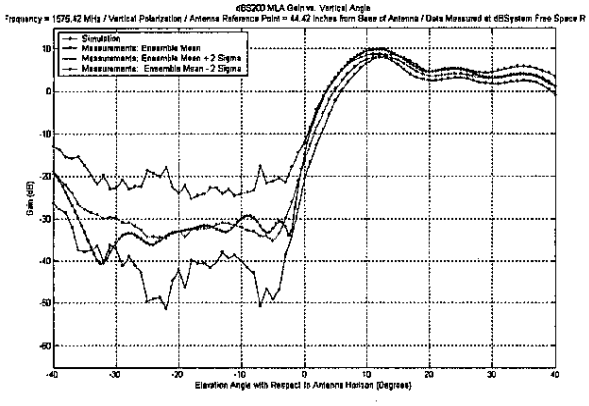

Figure 10. Gain pattern as a funtion of vertical angle for the MLA.

Figure 11 shows the gain D/U obtained from the simulated model, along with the mean and +/- two-sigma gain D/U obtained from the measurements.

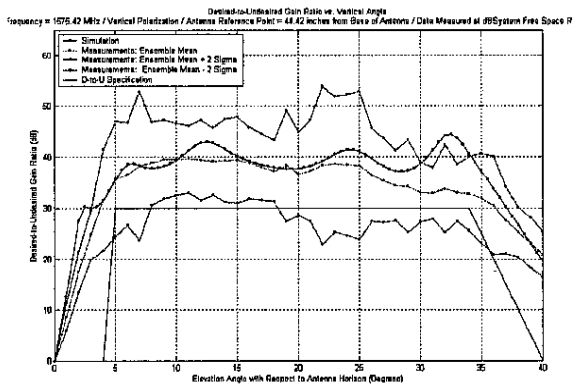

Figure 11. D/U gain as a funciton of elevation angle for the MLA.

It can be seen from Figure 11 that the modeled data agrees very well with the measurements between 4 and 30 degrees elevation, but falls outside the +/- two-sigma band between 1 and 3 degrees, and 30 and 34 degrees. The lack of exact agreement in the back lobes, specifically in the elevation angle region about -32 degrees, contributes to the D/U excursion.

It is important to characterize the phase variation of the MLA within its operating elevation angle range due to its large vertical aperture. Figure 12 shows the phase function obtained for modeled MLA along with that obtained from a measurement set (corresponding to Serial Number 041). Unlike in the gain D/U measurement case, wherein measurements corresponding to 20 different units were available, only one measurement set of the phase function was available. Figure 12 also plots the difference between the measured and the modeled phase as a function of elevation angle. It can be seen from the figure that the two agree to within 1 degree in the range of interest.

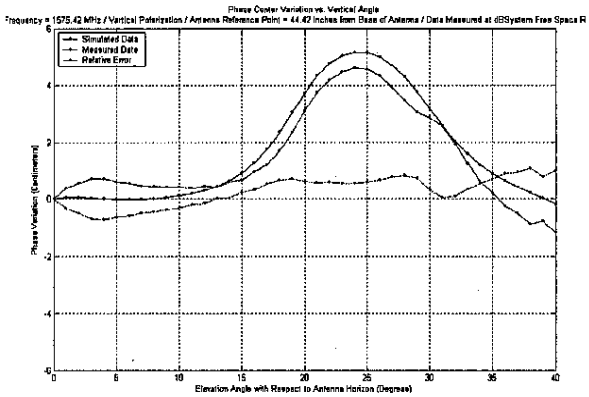

Figure 12. Phase variation as a funciton of elevation angle for the MLA.

Measurements from an actual MLA conducted at dB Systems Inc. in Utah are shown in Figures 3.3-3.5. Two MLA antennas, SN041 and SN055, were measured at dBSystems, Inc. for group delay measurements. SN041 was measured in August 2004, while SN055 was measured in October 2005. The procedure to measure the group delay from 0 degrees to 40 degrees in elevation angle took approximately three hours and considerable phase drift occurred over the measurement procedure between the group delay curves for SN041 and SN051.

Figure 13 shows the GD plots from the HFAM in comparison to the measurements for SN041 and SN055. The lossless model was able to predict the GD for SN041, while the lossy model gave closer results to the measurements for SN055. Although it is very difficult to match simulations and measurements for the GD, the two models provide a good predictive model for such corrections with a good confidence level. The maximum deviation for lossy model from measurements was approximately 4 cm around 30° in elevation, while for the lossless it was approximately 3 cm around 25°. The model clearly predicts the trends of the group delay measurements. However, the accuracy was predictable within 5 centimeters.

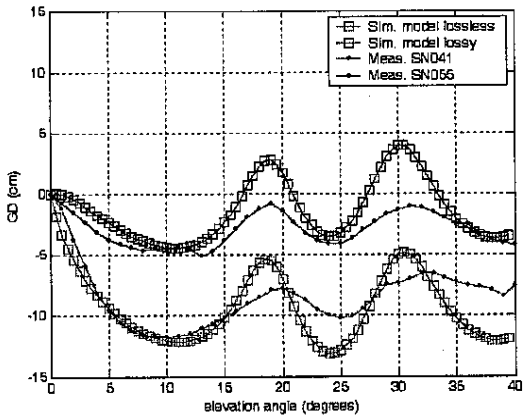

Figure 13: GD Simulation Results vs. GD Measurements for SN041 and SN051 of the MLA.

2.5 HZA HFAM Validation Results

Antenna gain as a function of elevation angle for the HZA is plotted in Figure 14 for both the derived model and the measurements obtained from the antenna range. It is seen from Figure 14 that there is good agreement between the two in the antenna main lobe, but significant discrepancies exist in the side and back lobes. The reasons for the disagreement are under investigation, and some of the potential reasons are listed below:

a. Minor variation in antenna dimensions between the modeled and physical structures. As the side and back lobes contain diminished energy levels, the regions are more sensitive to small geometric differences.
b. Variation in the properties of the modeled RF absorber from the physical.
c. Accuracy and repeatability of the measured phase.
d. Error from modeling the concave shaped reflector as a spherical section.
e. The inability to model coated conductors in FEKO. Owing to this the RF choke was modeled as three separate surfaces, with the outer ring being modeled as a dielectric sheet, and the inner ring as a perfect conductive layer. This approximation may be inaccurate.

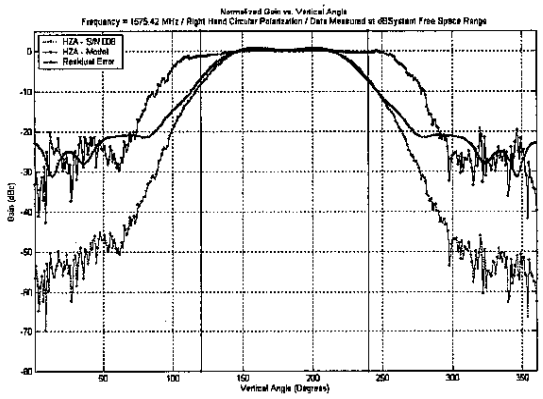

Figure 14. Gain pattern as a function of elevation angle for the HZA

The gain D/U ratio of the model along with that of the measurement set is shown in Figure 15. As the D/U is the ratio of the gain a positive elevation angle to that of the corresponding negative elevation angle, discrepancies in the side and back lobes, as discussed above, would affect the obtained values. This is seen in Figure 15, from which it is also noted that there are points in the elevation range in which the simulation does not meet the antenna specifications. Investigation of the mismatch between the measured and modeled gain patterns would shed light on the D/U mismatch as well.

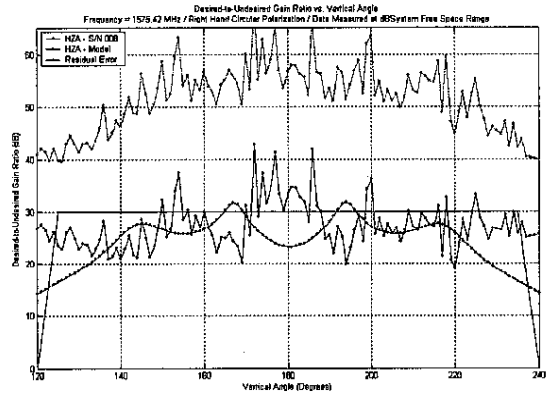

Figure 15. D/U gain as a function of elevation angle for the HZA

The phase variation in the vertical direction for the modeled HZA versus the measured HZA data is shown in Figure 16. Phase variation in the case of the modeled data is seen be between 0 and 3 cm, whereas that of the measured data is seen to be limited to 0.5 cm. This performance makes the measurements suspect, as the signal penetrates through RF absorbing material of varying thickness, which should affect the signal phase, but this behavior that is not seen in the measurements.

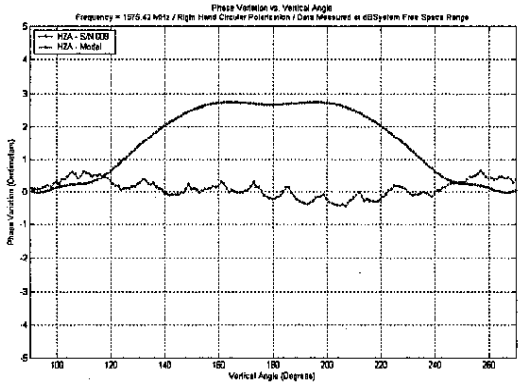

Figure 16. Phase variation as a function of elevation angle for the HZA

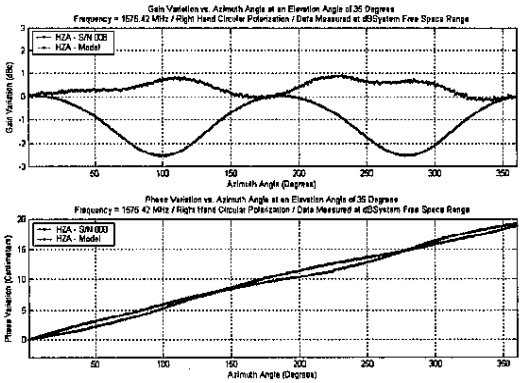

Figure 17. Gain and phase as a function of azimuth angle for the HZA (for elevation angle of 35 degrees).

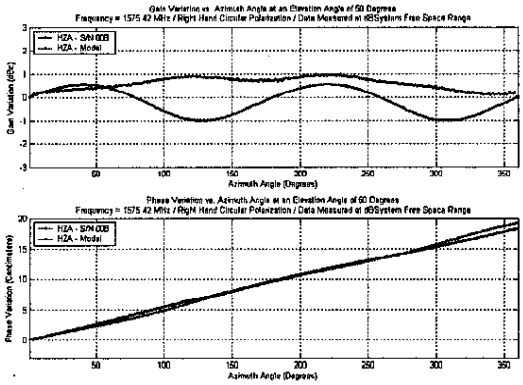

Figure 18. Gain and phase as a function of azimuth angle for the HZA (for elevation angle of 50 degrees).

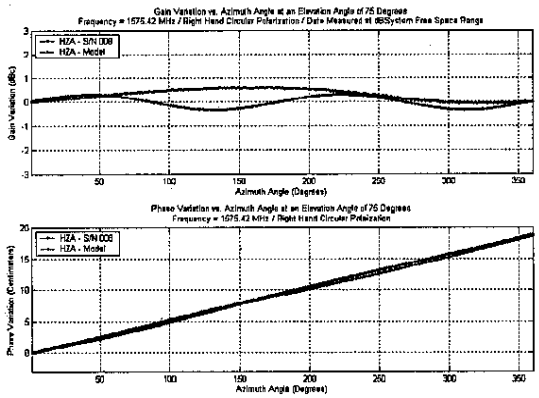

Figure 19. Gain and phase as a function of azimuth angle for the HZA (for elevation angle of 75 degrees).

The horizontal gain and phase patterns corresponding to elevation angles of 35, 50, and 75 degrees are shown in Figure 17, Figure 18, and Figure 19, respectively, from which good agreement between the model and the reference is seen. The horizontal gain patterns are seen to be omni-directional to within +/- 1 dB and the phase variation in the horizontal plane is seen to be circular, with the 360 degrees linearly progressing phase shift expected of an RHCP antenna. The GD was not calculated for the HZA because field data collections of the code-minus-carrier data from a GPS receiver connected to an HZA produced variations of less than 1 centimeter over its operational range in elevation angle.

3. Reference Receiver Site Data Collections with Dual-Frequency IMLA

A reference receiver site (RRS) was established at Oakland County International Airport located in Pontiac, Michigan in order to collect 24-hour continuous data from a dBs 260 L1/L2 MLA S/N 002 and HZA S/N 048. An L1/L2 diplexer is mounted in the pipe adapter so that one RF ports contains L1/L2 GPS signals from the L1/L2 MLA. In addition, a separate RF port contains L1/L2 GPS signals from the HZA. Both antennae were connected to OEM4 L1/L2 GPS receivers. The above configuration is illustrated in Figure 20 while an airport layout for the Oakland County International Airport indicating the location of the RRS at is provided in Figure 21.

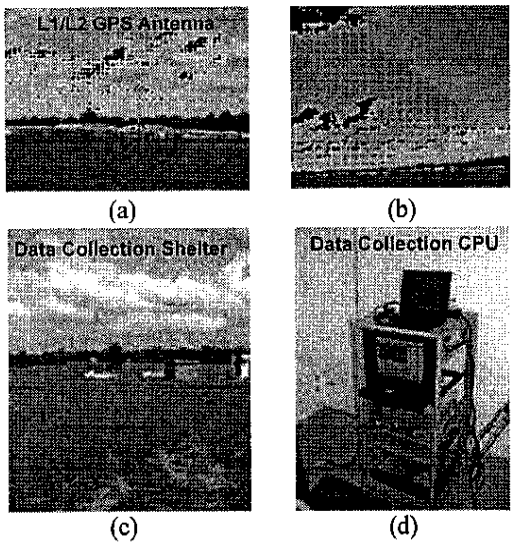

Figure 20: RRS at Oakland County International Airport Comprised of (a) dBS260 MLA and HZA, (b) Located in Front of Runway as Depicted with Airplan on Approach, (c) Data Collection Shelter, (d) Data collection CPU with 3 OEM4 L1/L2 WAAS GPS Receivers Connected to L1/L2 HZA, L1/L2 MLA, and L1/L2Pinwheel Antenna.

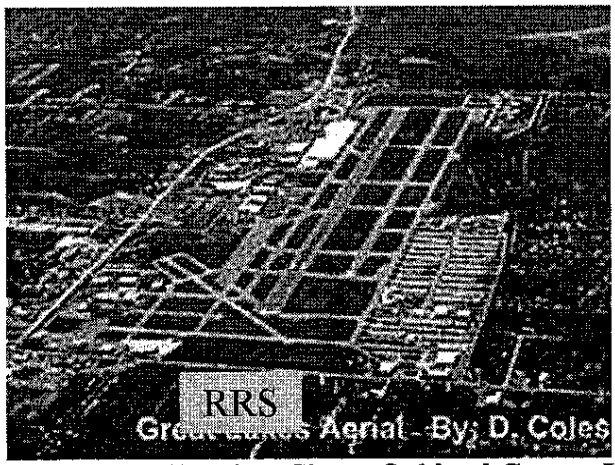

Figure 21: Location of Reference Receiver Site at Oakland County International Airport.

Five months of data were collected during the time period between July 30, 2004 and April 14, 2005. Initially, a 24-hour data collection over one day was collected and processed to monitor the L1 and L2 carrier-to-noise ratio performance from the MLA (Figure 22) and the HZA (Figure 23).

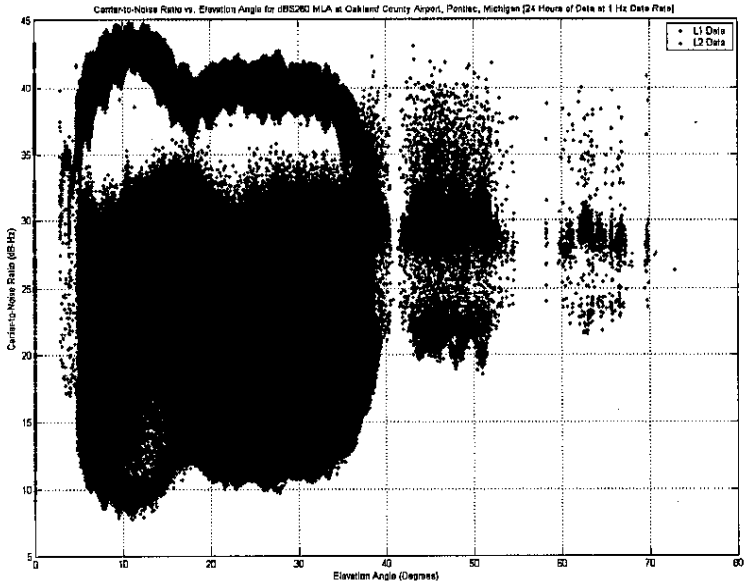

Figure 22: L1 and L2 Carrier-to-Noise Ratio Data over a 24-hour Period from dBS 260 MLA.

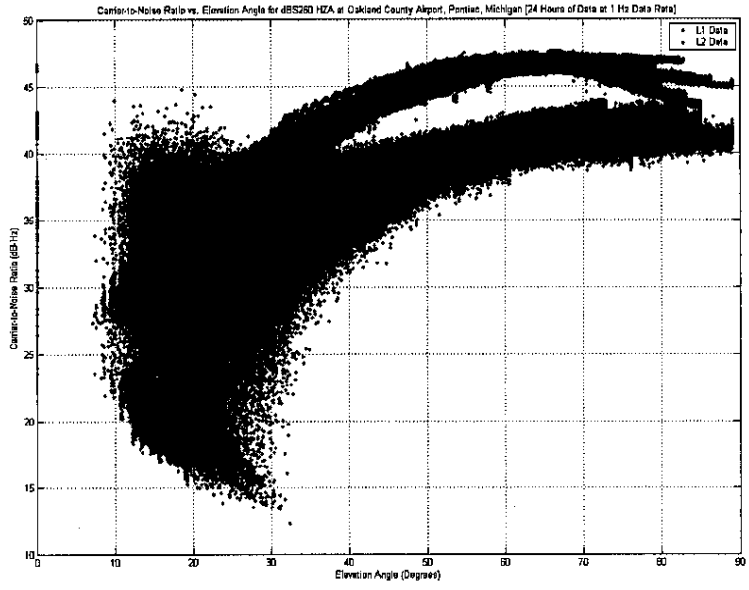

Figure 23: L1 and L2 Carrier-to-Noise Ratio Data over a 24-hour Period from HZA.

In summary, the L2 carrier-to-noise ratio measurements from the MLA were unacceptable and the L2 carrier-to-noise ratio measurements from the HZA were acceptable but possessed lower mean values and higher standard deviations than its corresponding carrier-to-noise ratio measurements on L1. As a result, the L1/L2 Pinwheel antenna connected to a L1/L2 OEM4 GPS receiver was used in order to remove the effects of the ionosphere from the L1 data out of the MLA due to a lack of L2 data from this same antenna. Several low noise amplifiers were tried in order to improve the L2 performance of the MLA with no success.

3.1 Dual Frequency MLA Performance

Three hundred and sixty five days of GPS data were collected from the dBS 260 MLA. Code-minus-carrier data was calculated from the resulting L1 code-phase and L1 carrier phase measurements from the dBS 260 MLA. The ionosphere was removed from the L1 and L2 data collected from L1/L2 Pinwheel Antenna/L1/L2 OEM4 GPS receiver pair. The L1 CMC mean and L1 CMC standard deviation when using sample sizes of one day is illustrated in Figure 24. Similarly, Figure 25 shows the L1 CMC mean and the L1 CMC standard deviation when using sample sizes of one month. Figure 24 and Figure 25 show the same trends with the results in Figure 25 being smoother. The results clearly indicate that a correction table is needed to remove the large biases introduced to the L1 code phase measurements by the dBS 260 MLA. Furthermore, no L2 data was available from this antenna due to its poor performance. Furthermore, Figure 26 shows the percentage of data used each day in the CMC processing. It is very low due the location of the antenna in front of the runway. Approximately, 300 landings per day occur at this runway and on aircraft approach the high gain of the MLA reflects of the aircraft and causes loss of lock in the receiver.

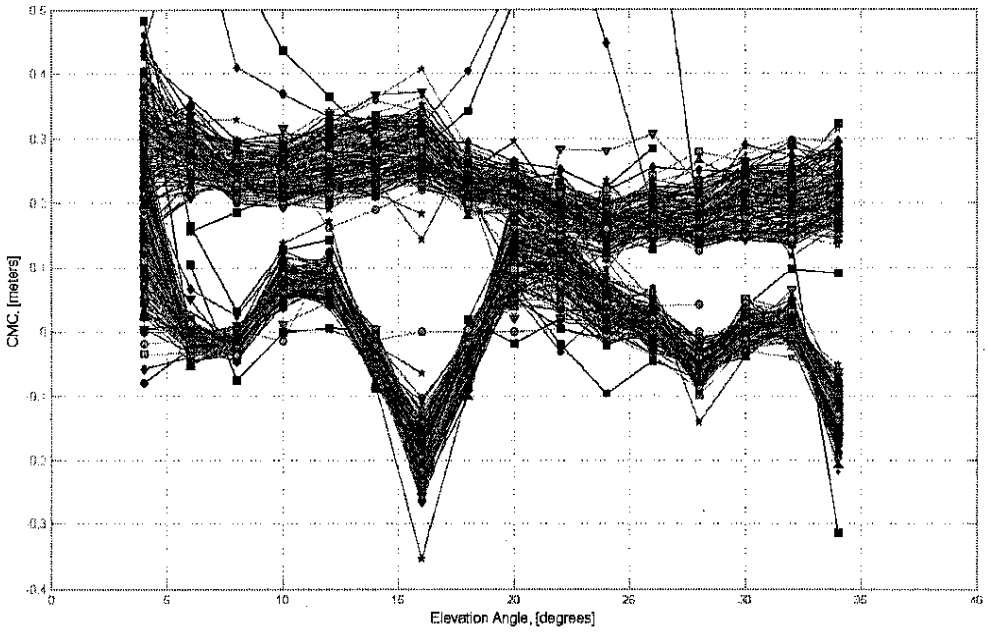

Figure 24: L1 CMC Mean and Standard Deviation Results from L1/L2 dBS260 MLA Averaged Each Day over 165 Days of Data.

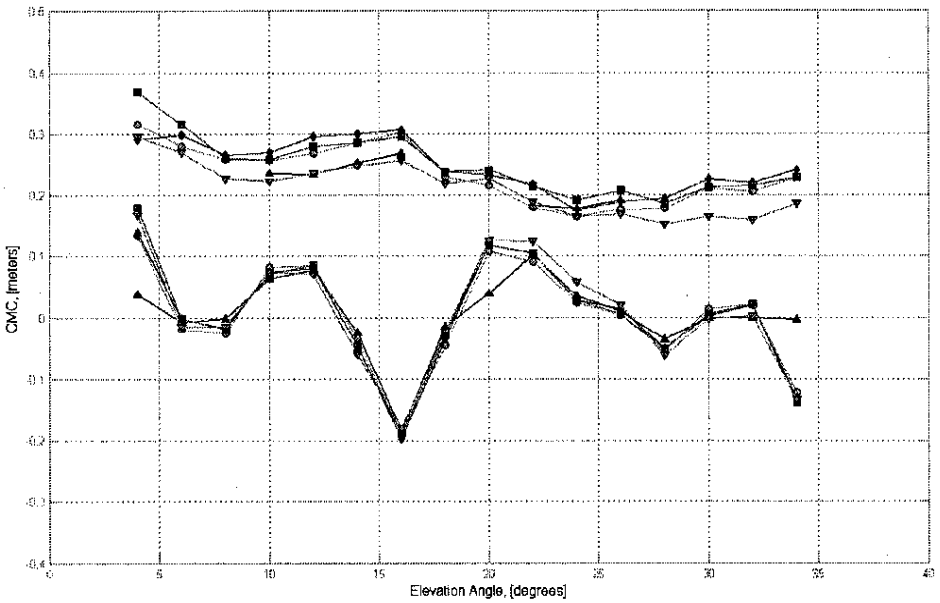

Figure 25: L1 CMC Mean and Standard Deviation Results from L1/L2 dBS260 MLA Averaged Each Month over 165 Days of Data.

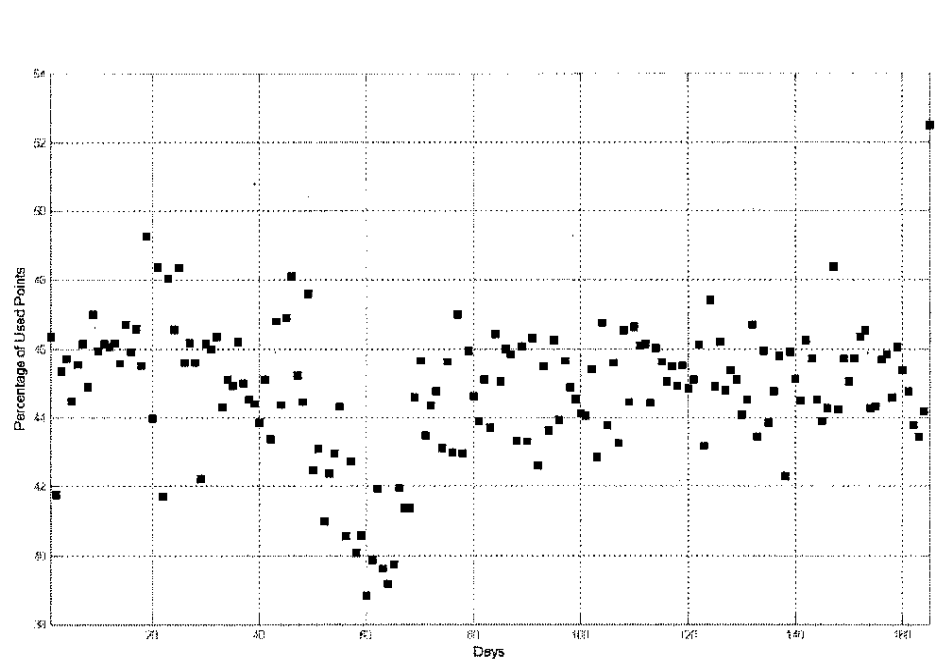

Figure 26: Percentage of Data Used from dBS 260 L1/L2 MLA for Each of the 165 Days.

3.2 Dual Frequency HZA Performance

The L1 CMC performance (Figure 27 and Figure 28) and L2 CMC performance (Figure 29 and Figure 30) from the HZA antenna was within +/- 2.5 cm from 35° - 70° in elevation angle in terms of mean values. Figure 27 and Figure 28 show the L1 CMC mean and standard deviation performance vs. elevation angle when combining data each day and each month, respectively. While Figure 29 and Figure 30 show the L2 CMC mean and standard deviation performance vs. elevation angle when combining data each day and each month, respectively. Furthermore, Figure 31 shows the percentage of data utilized from the HZA was close to 100% on all days with a few exceptions.

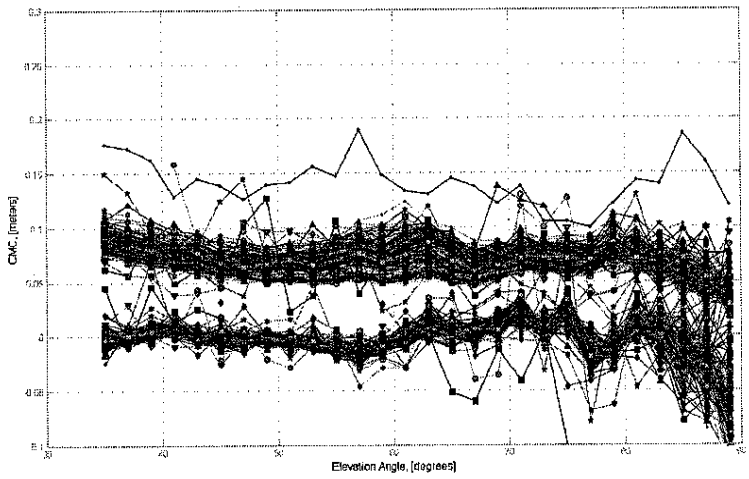

Figure 27: L1 CMC Mean and Standard Deviation Results from L1/L2 HZA Averaged Each Day over 165 Days of Data.

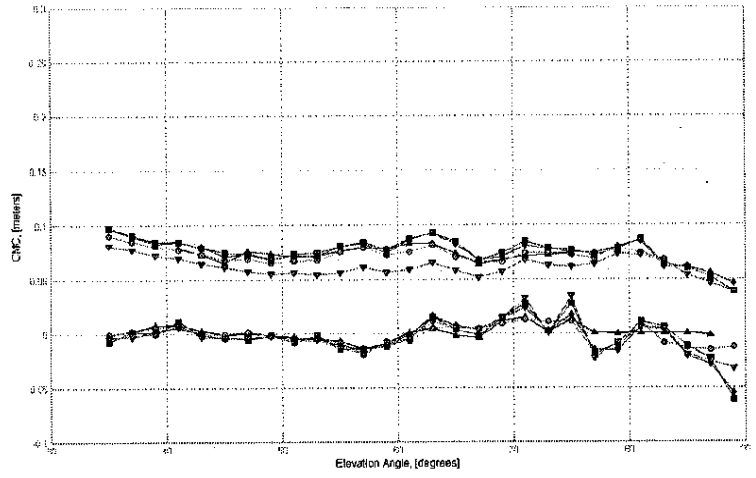

Figure 28: L1 CMC Mean and Standard Deviation Results from L1/L2 HZA Averaged Each Month over 165 Days of Data.

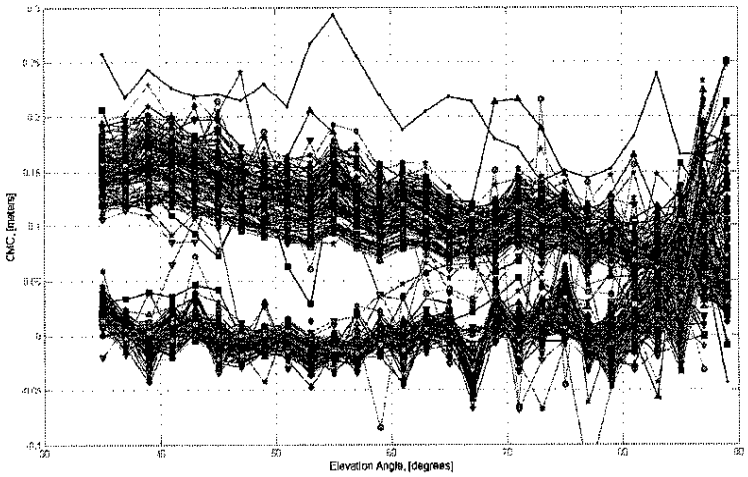

Figure 29: L2 CMC Mean and Standard Deviation Results from L1/L2 HZA Averaged Each Day over 165 Days of Data.

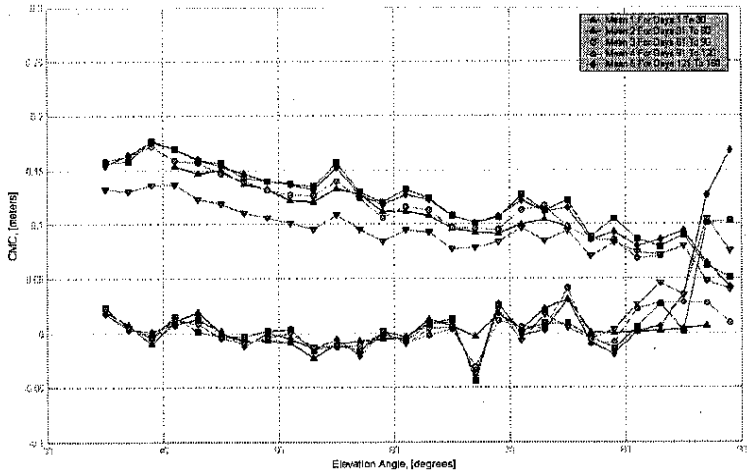

Figure 30: L2 CMC Mean and Standard Deviation Results from L1/L2 HZA Averaged Each Month over 165 Days of Data.

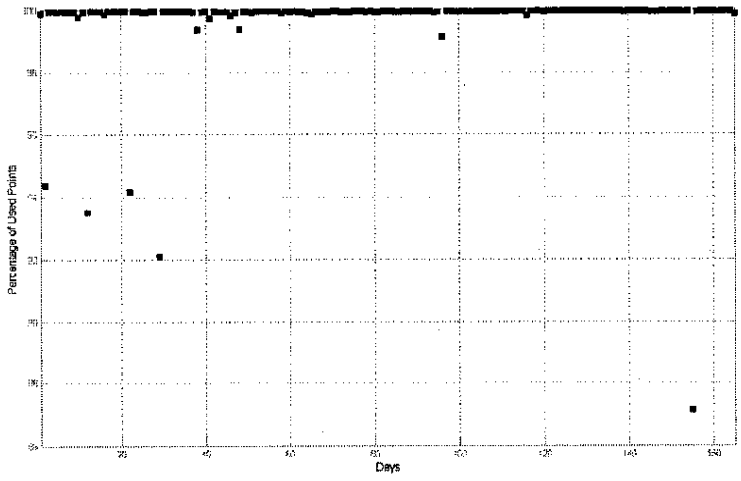

Figure 31 Percentage of Data Used from HZA A for Each of the 165 Days.

4. Anti-Jam Approaches for Multipath Limiting Antenna (MLA)

The multipath limiting antenna (MLA) is a proposed component in the Local Area Augmentation System (LAAS) ground architecture. The MLA was designed to mitigate errors due to ground multipath by creating a radiation pattern that exhibits a desired-to-undesired (D/U) gain ratio in excess of 35dB. Radio frequency interference (RFI), both intentional and/or unintentional, poses significant threats for LAAS to meet Category II/III availability requirements. This threat can be minimized by increasing the satellite signal transmitting power, creating additional civil frequencies, and/or by developing anti-jam antenna technologies. This effort investigated two distinct approaches of incorporating null-steering capability into the MLA.

4.1 Investigated Approaches

The first approach is referred to as the Vector Weighting Method (VWM) while the second approach is referred to as Beam Pattern Combining (BPC). The two approaches are described below.

4.1.1 Vector Weighting Method (VWM)

In the VWM, the inputs/outputs of the antenna array are weighted so that a null is created in the direction of interference. The weighting is done by processing the incoming satellite signals at baseband in order to identify the direction of interference. Once the direction of interference is known, the radiation pattern is then adapted to create a null in that direction. The resulting pattern is the multiplication of the array manifold vector that incorporates the spatial characteristics of the fixed array with the optimum weighting vector that is created to reflect the null creation mechanism (Figure 32).

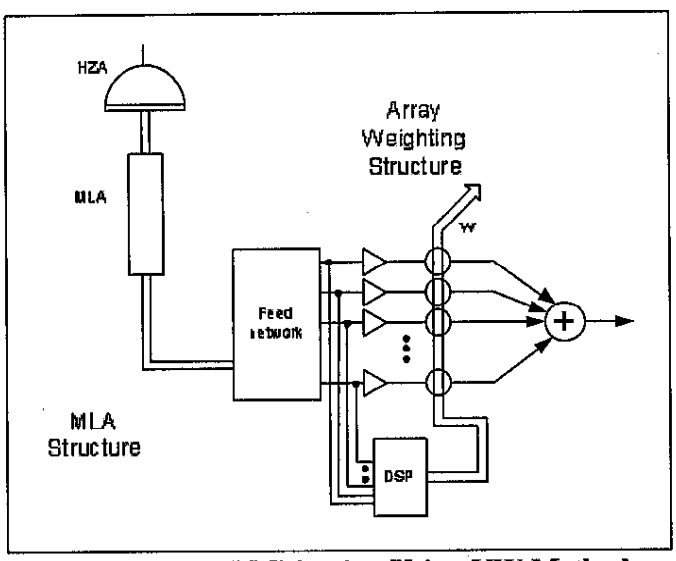

Figure 32: RFI Mitigation Using VW Method.

4.1.2 Beam Pattern Combining (BPC)

The BPC approach is divided into two stages. The first stage generates a narrow beam in the direction of the interfering signal using a planar patch antenna array. And the second stage

involves subtraction of the narrow beam, determined in stage 1, from the radiation pattern of the MLA. The subtraction is done in baseband via a digital signal processor.

4.2 Simulation Results of VW and BPC

The performance of the VWM and BPC approaches were quantified by assessing the null depth, null width, desired-to-undesired gain ratio (D/U), phase center variation (PCV) and group delay (GD) for a source of interference at a specified elevation/azimuth direction by assessing these parameters at the radiation pattern level. Next, a simulation was conducted in which the GPS satellite signal and a CWI source at a particular elevation/azimuth angle were created. The appropriate fixed MLA radiation pattern, radiation pattern for the VWM, and the radiation pattern for the BPC were incorporated into the simulation. A simulated GPS signal at IF was then processed through each of these patterns to gauge their influence on the GPS signal in order to assess the impact on the satellite signal's carrier-to-noise ratio (C/N0) levels.

4.2.1 Null Depth and Width

Table 3 and Table 4 show the results for the VWM and BPC approaches, respectively. For the VWM (Table 3) the resulting half power beam-width in both the elevation and azimuth planes are calculated for sources of interference arriving at various elevation angles. The compelling result in Table 3 is that a null spans 360° in the azimuth direction, which is negative since it prevents tracking GPS satellites at the same elevation angle within this azimuth band, albeit not in the direction of the source of interference. However, the null depth for the VWM is in excess of -20.3 dB over all elevation angles in the range from 5° to 35°.

Table 3: VW null steering vs. elevation angle.

θ	$HPBW_\theta$ (deg)	$HPBW_\phi$ (deg)	SLL_θ (dB)	SLL_ϕ (dB)	Depth (dB)
5	3	360	-14.5	N/A	-35.2
10	10.3	360	-8.2	N/A	-29.1
15	9.8	360	-13.9	N/A	-22.7
20	5.9	360	-21.6	N/A	-20.3
25	11.1	360	-23.7	N/A	-50.2
30	7.2	360	-27.4	N/A	-45
35	4.5	360	-21.5	N/A	-35

Table 4 shows similar results but for a slightly different scenario. First, it assumes the source of interference arrives at an elevation angle of 20° and an azimuth angle of 45°. Next, it determines the half power beamwidth in both planes as a function of the size of the planar array since that directly determines the null width in both planes. The resulting null width in both planes is superior to those produced with the VWM. Specifically, the half power beam-width is limited to 37° for an 8x8 planar array. However, the null depth for the BPC performs much worse than that produced by the VWM.

Table 4: HPBW and SLL as a Function of the Patch Array Elements for Interferer Located at $\theta=20^0$ and $\phi=45^0$ for BPC.

Patch elements	Beam $HPBW_\theta$ °	Beam $HPBW_\phi$ °	Beam SLL_θ (dB)	Beam SLL_ϕ (dB)	Pattern Null Depth (dB)
8 x 8	13.94	37.2	-20.4	-12	-7.7

9 x 9	12.4	32.9	-21.3	-13.2	-8.83
10 x 10	11.4	29.45	-22.1	-14.3	-11.05
11 x 11	10.1	26.7	-22.4	-15.3	-11.1
12 x 12	9.3	24.4	-23	-16.6	-13.1
13 x 13	8.5	22.5	-23.1	-17	-13.3
14 x 14	7.9	20.7	-23.5	-17.8	-11.68
15 x 15	7.3	19.2	-23.7	-18.1	-14.47
16 x 16	6.8	17.9	-24	-18.6	-14.6

4.2.2 Desired-to-Undesired Gain Ratio

The D/U gain ratio for the VWM and PRC approaches when subject to an interfering signal at an elevation angle of 20° is shown in Figure 33. It is still important for the MLA to mitigate the multipath error due to ground multipath for all tracked satellites outside the direction of the interfering source. Figure 33 shows that the D/U gain ratio produced by the VWM approach is inferior to the D/U gain ratio produced by the BPC approach over the operational range of elevation angles of the MLA.

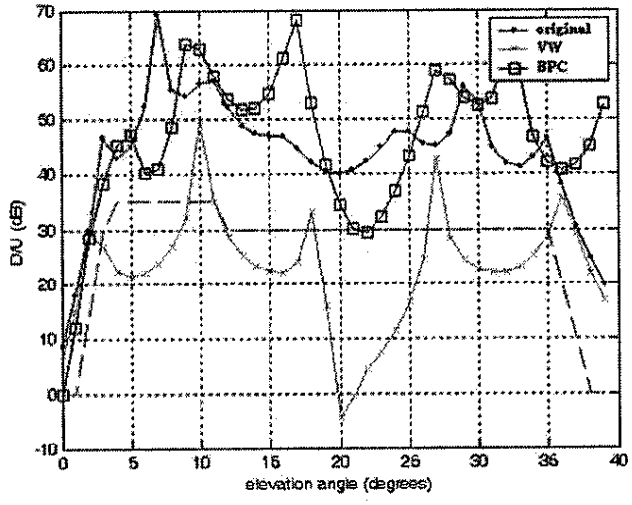

Figure 33: Desired-to-Undesired Gain Ratio for 14-Element MLA for VW and BPC Methods.

4.2.3 Phase Center Variation

In a similar fashion, the PCV curves for the VWM (Figure 34) and the BPC (Figure 35) approaches for an interference source at a distinct elevation angle are important since the accumulated carrier phase observables for all tracked satellites are corrupted by this error. This error can be removed in software via a correction table as long as it is known beforehand. Figure 34 and Figure 35 show the difference between the PCV curves for the VWM and the original MLA pattern, and the BPC and the original MLA pattern, respectively. It would simplify matters if the resulting PCV curve matched the PCV curve for the original MLA except in the direction of the source of interference, which is what happens for the BPC approach (Figure 35).

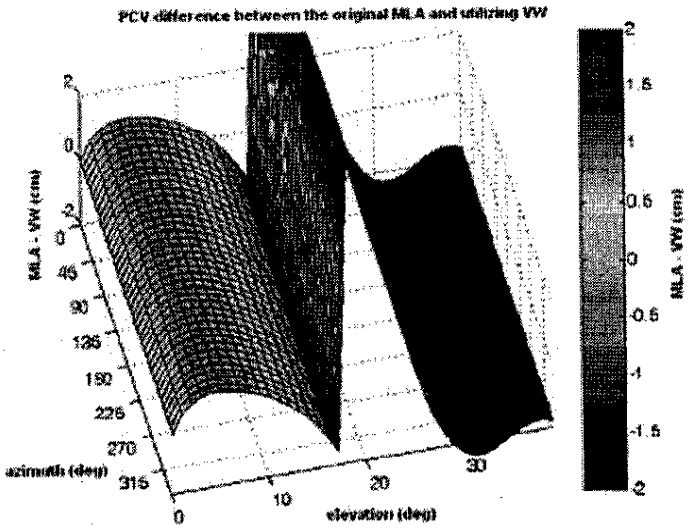

Figure 34: PCV Difference between Original MLA Pattern and VW Method for an Interference Source at a Particular Elevation Angle.

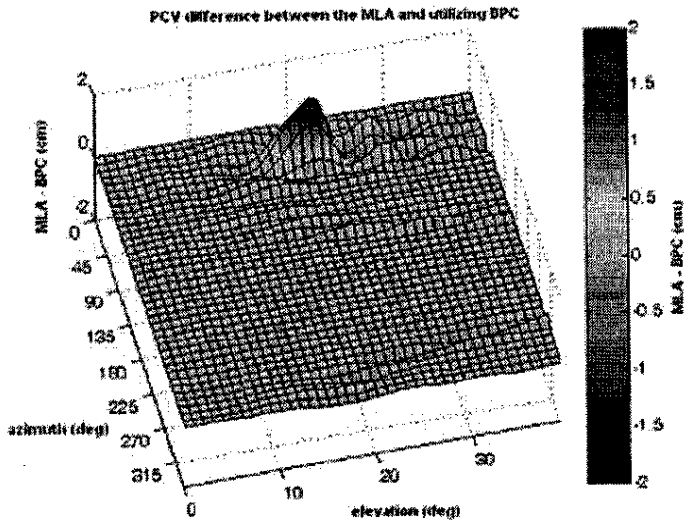

Figure 35: PCV Difference between Original MLA Pattern and BPC Method for an Interference Source at a Particular Elevation Angle.

4.2.4 Group Delay

The same rationale as explained for the PCV curve applies to the GD curve. It can be seen that the VWM approach (Figure 36) produces a group delay curve that differs significantly from the group delay curve of the original MLA. However, the GD curve for the BPC approach (Figure 37) is very close to the GD curve of the original MLA except in the direction of interference.

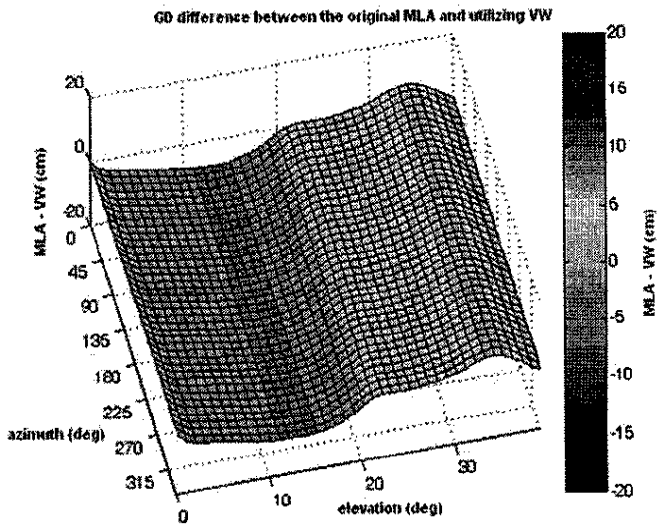

Figure 36: GD Difference between Original MLA Pattern and VW Method for an Interference Source at a Particular Elevation Angle.

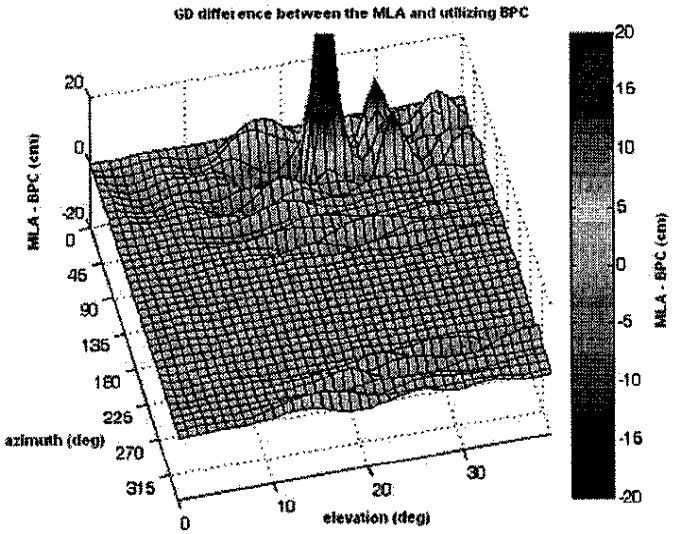

Figure 37: GD Difference between Original MLA Pattern and BPC Method for an Interference Source at a Particular Elevation Angle.

4.2.5 Carrier-to-Noise Ratio

Research was also conducted to better understand the estimated C/N0 level for a GPS satellite signal in presence of a continuous wave source of interference and a pulsed interfere. In both scenarios the interference occurred in a particular elevation/azimuth direction. It was then assumed that a GPS signal arrived at a particular elevation/azimuth direction. Specifically, 5 elevation bins and 23 azimuth bins resulting in 115 elevation/azimuth bins. The GPS signal and the interfering signal were produced at an intermediate frequency and incorporated the impact of the complex radiation pattern for the MLA's original pattern and null-induced pattern. The CN0

estimate was then calculated. The procedure is depicted in (Figure 38) while the results for CWI and PPS are shown in Figure 39 and Figure 40, respectively.

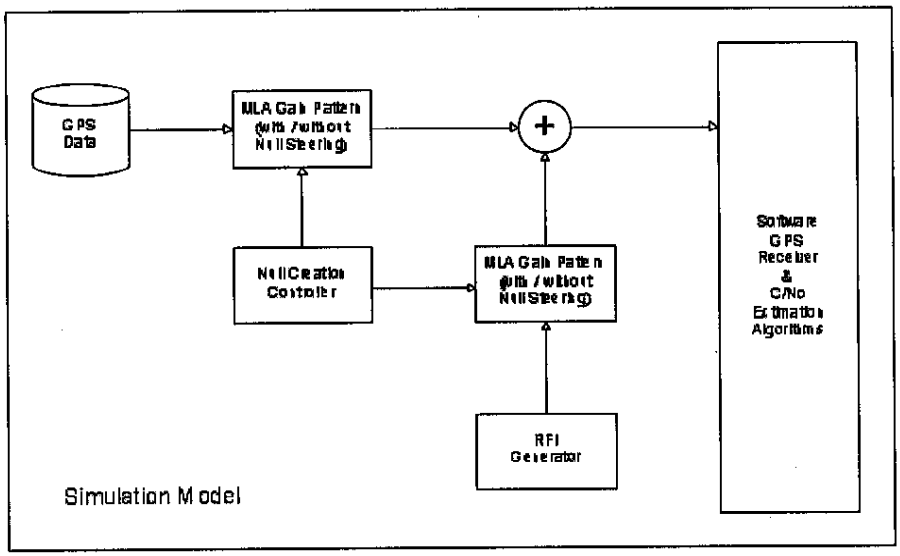

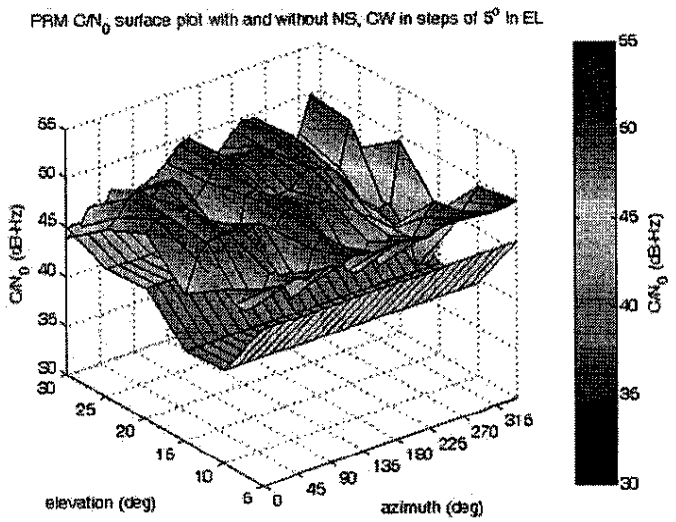

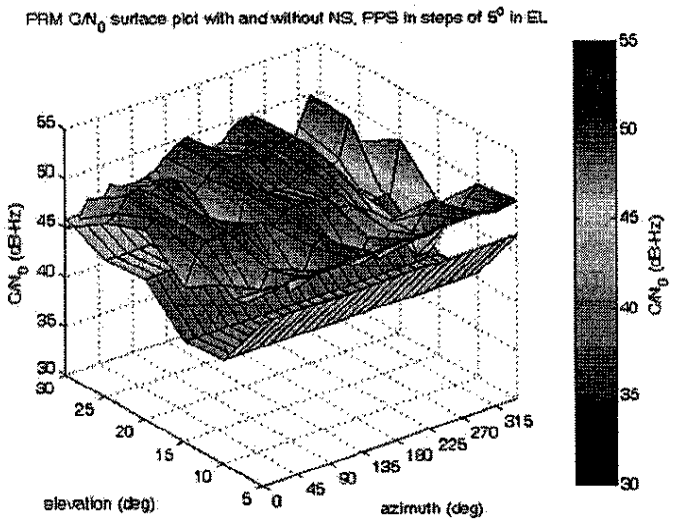

Figure 40: Illustration of Carrier-to-Noise Ratio Levels in the Presence of a Pulsed Interferer With and Without Null-Steering in MLA.

REFERENCES

1 **Daniel N. Aloi**, Mazen Alsliety, and Sai Kiran, *"The Development and Validation of a High-Fidelity Electromagnetic Model of the Integrated Multipath Limiting Antenna,"* Institute of Navigation, ION Annual Meeting 2004, 7-9 June 2004, Dayton, Ohio.

2 **Daniel N. Aloi** and Sai Kiran, *"Failure Mode Analysis of Multipath Limiting Antenna,"* Institute of Navigation, Institute of Navigation GNSS 2004, 21-24 September 2004, Long Beach, California. (Best Paper Award)

3 Bryce Thornberg, Mark Dickenson and **Daniel N. Aloi**, *"LAAS Multipath Limiting Antenna (MLA) Performance Testing and Analysis,"* Institute of Navigation, Institute of Navigation National Technical Meeting 2005, 21-24 January 2005, San Diego, California.

4 Mohammad Sharawi and **Daniel N. Aloi**, *"Comparative Analysis of Two Null-Steering Approaches for the Multipath Limiting Antenna for LAAS,"* I.E.E.E. PLANS 2006/ION NTM 2006, Monterrey, CA. January, 12-15, 2006.

5 Mohammad Sharawi and **Daniel N. Aloi**, *"Radio Frequency Interference Mitigation via Null-Steering for the Multipath Limiting Antenna Array in Local Area Augmentation Systems,"* Proceedings of the 2006 I.E.E.E. Electro/Information Technology Conference (EIT 2006), Lansing, Michigan, May 7-10, 2006, Page(s): 137-141. Digital Object Identifier 10.1109/EIT.2006.252110.

6 Mohammad Sharawi and **Daniel N. Aloi**, *"C/No Estimation in a GPS Software Receiver in the Presence of RF Interference Mitigation via Null Steering for the Multipath Limiting Antenna,"* I.E.E.E. GLOBECOMM 2006, 27 November – 1 December, 2006, San Francisco, California.

7 Mohammad Sharawi, Dennis Akos, and **Daniel N. Aloi**, *"GPS C/N0 Estimation in the Presence of Interference and Limited Quantization Levels,"* I.E.E.E. Transactions on Aerospace and Electronic Systems, Volume 43, Issue 1, January 2007, Page(s): 227-238. Digital Object Identifier 10.1109/TAES.2007.357129.

8 Mohammad Sharawi and **Daniel N. Aloi**, *"Null Steering Approach with Minimized PCV and GD for Large Aperture Vertical Antenna Arrays,"* I.E.E.E. Antennas and Propagation, Tentative - July 2007, Volume TBD, Number TBD, ISSN TBD, pp. TBD.

9 Mohammad Sharawi, *"Radio Frequency Interference Mitigation Methods Applied to the LAAS Multipath Limiting Antenna for System Availability Improvement,"* Doctoral Dissertation, Department of Electrical and Computer Engineering, Oakland University, Rochester, Michigan, December 2006.